ORIGINAL ARTICLE

Effect of bottom sheet thickness on weld properties during laser lap welding of aluminum and copper

Mounarik Mondal[1,2] · Joonghan Shin[1,3,4] · Donkyoung Lee[1,3,4,5]

Abstract

Continuous laser lap welding for a dissimilar combination of aluminum (Al) and copper (Cu) was achieved successfully. The successful welding was achieved by varying laser power between 500 and 900 W with an interval of 100 W, whereas the variation in welding speed was maintained between 10 and 45 mm/min with an increment of 5 mm/min. A combination of various laser power and weld speed generated a broad range of volume energy inputs, among which acceptable welding with no macroscopic defect could only be generated between 1.81 and 7.64 kJ/mm^3. The volume energy required to achieve successful welding increased with the increase in bottom Cu sheet thickness. The joint's mechanical properties were significantly enhanced for thicker bottom Cu sheets as the welding was carried out at a higher volume of energy achieving higher depth of penetration of 0.65 mm in case of 1.5-mm bottom Cu sheet thickness. Lap shear tensile tests and Vickers's microhardness testing confirmed the abovementioned results as the highest breaking load of 373.79 N, and Vicker's hardness of 350 Hv inside Al and 750 Hv inside Cu was obtained. Furthermore, SEM results on the weld cross sections showed that welds with thicker bottom Cu sheets exhibit a higher penetration depth and lower top weld bead. Detailed electron microscopy and spectroscopy revealed the formation of hard intermetallic compounds (IMCs) inside the weld zone due to the Cu diffusion inside the weld. They correlated well with the measured mechanical and electrical properties. Electron back-scattered diffraction (EBSD) revealed a sudden concentration of high-angle boundaries (HAB) inside the weld, confirming the presence of hard IMCs. Inside the weld, most of the grain boundaries transformed into HAB, which explains the joints' enhanced mechanical properties.

This work was done when Mounarik Mondal was working in Kongju National University.

✉ Donkyoung Lee
  ldkkinka@kongju.ac.kr

1 Department of Mechanical and Automotive Engineering, Kongju National University, Cheonan, Republic of Korea 31080

2 Department of Advanced Materials Engineering, Dong-Eui University, Busan, Republic of Korea 47340

3 Department of Future convergence Engineering, Kongju National University, Cheonan, Republic of Korea 31080

4 Global Institute of Manufacturing Technology (GITECH), Kongju National University, Cheonan, Republic of Korea 31080

5 Center for Advanced Powder Materials and parts of Powder (CAMP), Kongju National University, Cheonan, Republic of Korea 31080

1 Introduction

The challenge of producing safe and energy-efficient structures in modern manufacturing while meeting environmental policies is significant. A single component made of a single material cannot provide all the necessary optimal properties at its best. Metals such as steel (Fe) and copper (Cu) have high strength and comparable conductivity but are also heavy. In contrast, aluminum (Al) and magnesium (Mg) are lightweight and conductive, but their strength is relatively low. Although various advanced composites and new-grade alloys are being developed to address this challenge, the cost of these materials can increase manufacturing expenses. Thus, to overcome the abovementioned challenges, most industries manufacture multi- or bimetallic structures. The pair is chosen based on the materials' service condition and counterbalancing properties. Al/Cu, Al/Fe, Al/Mg,

and Fe/Cu are some of the most common bimetallic couplings applied for various applications [1–4].

Al and Cu are excellent heat and electricity conductors with good corrosion resistance and mechanical properties. Hence, they find their applications in power generation, petrochemical industries, nuclear plants, aerospace, and electronic components. However, despite its many advantages, the high price and heavy mass of copper can increase a structure's weight and manufacturing cost. In contrast, aluminum is almost 1/4 of the mass of copper and is comparatively cheaper. Thus, incorporating Al into a structure can significantly reduce its weight and manufacturing cost. Hence, a structure that includes bimetallic Al-Cu coupling can provide all the advantages of both materials while counterbalancing the disadvantages of Cu [5–9].

Stringent air pollution laws have been implemented globally to combat the growing effect of global warming. Among all industries, the transportation industries of various countries have opted to incorporate green energy sources. Among all other industries, it is estimated that the transportation sector alone contributes more than 80% of harmful emissions. Since 2020, the European Union has aimed to limit emissions from newly manufactured cars to 95 g CO_2/km. Additionally, 12% of total CO_2 emissions are produced from fossil fuel–fired automotive vehicles [10, 11], leading to an increased demand for electric vehicles (EVs) and hybrid electric vehicles (HEVs).

Due to high energy density, volumetric power, open-circuit voltage, and ease of production, lithium-ion battery packs are the most desired for powering EVs and HEVs. These battery packs contain many battery cells that must be assembled together and joined in robust mechanical and electrical joints. Mainly in this battery pack for current collectors from the cells, aluminum and copper are commonly used as cathode and anode, or bus bars; in some cases, the tabs for cells are made up of steel too. Since the functions of each of these components are different, their thicknesses may vary. Hence, joining battery cells presents several challenges, such as welding highly conductive and dissimilar materials, joining multiple sheets, and varying material thickness combinations [12–14].

The metallurgical joining of any dissimilar combinations of metals, including Al-Cu, is only possible by generating intermetallic compounds (IMC), which actually reduces the welding quality in terms of mechanical properties and electrical conductivity. The difference in thermomechanical and physical properties, such as melting point, density, linear expansion coefficient, and low solid solubility, creates severe challenges while welding Al and Cu. Conventional arc welding methods such as inert tungsten gas (TIG) arc welding and inert metal gas (MIG) arc welding generate IMCs even in higher amounts inducing brittleness inside the weld and are mostly being avoided. Due to the widespread heat sources, conventional arc welding widens the weld bead, reducing the penetration depth and inducing a soft heat-affected zone (HAZ). Furthermore, this softened HAZ can reduce the strength of the base material of the welded structure [15–17]. Hence, researchers reported using a separate interlayer or different filler materials while performing conventional arc welding to reduce IMCs [18, 19]. In the reduction of heat input, modified TIG and MIG process such as cold metal transfer (CMT) has been reported by various researchers. By applying the cold metal transfer, Cai et al. [20] joined Al and Cu with AA4043 wire. He reported forming a thin Al single bond Cu eutectic phase and $CuAl_2$ and CuAl IMC during the joining process. Fan et al. [21] plasma arc weld brazed Al and Cu using SiO_2 nanoparticles with the formation of thin $CuAl_2$ IMC. Feng et al. [22] used $AlCu_5$ filler wire and carried out CMT to join aluminum plates with copper. A continuous intermetallic compound layer composed of Al_4Cu_9, Al_2Cu_3, and Al_2Cu is formed at the interface. However, the growth of the Al_2Cu IMC layer was the thickest.

The most commonly used solid-state joining methods to achieve Al-Cu joining are friction welding, friction stir welding, diffusion bonding, and roll bonding. Although these methods join the material at a lower melting point, they often result in the formation of brittle intermetallic compounds (IMCs) such as $CuAl_2$, Cu_9Al_4, CuAl, and Al_3Cu, in small amounts or thinner widths [23–26]. Many researchers claim that solid-state joining performs comparatively better than conventional fusion welding due to its lower heat input and absence of solidification defects, making it an attractive option [27, 28]. However, its applicability for outdoor industrial purposes is questionable due to the complex setup and slow processing. Furthermore, solid-state joining involves high mechanical force, resulting in friction with the workpiece, wear, and deformation of the tool. As a result, manufacturing costs increase significantly. Therefore, a faster process with a simple setup that forms fewer IMCs is still desired for almost all dissimilar welding processes [29, 30].

Recently, laser technology has gained popularity in manufacturing sectors because of its fast processing time and high energy density, which can be achieved with simple and economical equipment. In addition, it has some additional advantages such as remote control, high precision, and no requirement of secondary media assisting the process. The high energy density and fast processing time result in thin weld beads with fine microstructures inside the weld, which further reduces the chances of forming brittle IMCs and enhances mechanical properties and electrical conductivity within the joints. Moreover, it reduces the width of the HAZ and avoids weakening the base material during welding. The laser welding can be carried out both in conduction mode or keyhole mode, providing flexibility for joining dissimilar materials,

particularly in Al-Cu joining where strength or conductivity is a priority. Considering these advantages, it can be concluded that laser beam welding is an efficient method for welding Al-Cu in a dissimilar configuration [31–34].

To date, several studies have been conducted on Al-Cu laser welding using beam oscillation or pulsed lasers to find the effects of the laser welding parameters on welding properties. Gedicke et al. [35] compared the weld qualities of dissimilar thickness joining of Al and Cu with and without beam modulation. They concluded that beam modulation generates more contact area between Al and Cu. Dimatteo et al. [36] used continuous laser welding with spatial beam oscillation to join Al and Cu by altering the top and bottom sheet position and achieved the highest possible breaking load of 100 Kgf using optimized process parameters. Mathivanan et al. [37] studied the combined effect of the beam oscillation and shaping of lasers on the overlap welding of Al and Cu. The researchers concluded that a discontinuous joining with a higher amount of IMCs and a continuous joint with lesser IMCs both provided good mechanical strength. Lerra et al. [38] studied the effect of pulse shape and separation distance for joining Al and Cu and reported pulse shaping with material pre-heating generated better mechanical strength and electrical resistance.

To the best of the author's knowledge, no previous studies have investigated the effect of increasing the bottom Cu sheet thickness on the required laser energy and mechanical, electrical, and microstructural properties of dissimilar Al-Cu welding using the continuous laser. Thus, in this study, Al-Cu dissimilar joining was carried out with continuous laser by varying the bottom Cu sheet thickness to observe the change in the required volume energy, laser parameter input, and weld property output. In all cases, the Al plate was always kept on top. Increased bottom Cu sheet thickness, allowed high volume energy for defect-free welding, and greater penetration depth, leading to increased breaking load and high microhardness values, could be achieved. Optical and electron microscopy of the successful joints revealed morphological changes within the weld and penetration of aluminum into the copper. EDS line scanning clarified the Al-Cu mixture inside the weld zone, with near-similar Al and Cu content indicating the formation of some IMCs. Similar phenomenan is also confirmed again by the EDS point analysis. The EBSD analysis revealed the grain structure and excessive formation of high-angle boundaries, especially near the Al-Cu interface, ensuring the formation of hard IMCs.

2 Experimental procedure

2.1 Materials and methods

A single-mode continuous wave (CW) Yb: fiber laser with a wavelength of 1080 nm and a spot size of 100 µm was applied to lap weld 99.60% pure Al 1060 alloy and pure oxygen-free Cu UNS C10100. Both the samples were cut into rectangular pieces of a length of 50 mm and a width of 10 mm. To carry out the welding, the plates were overlapped for about 10 mm and tightly clamped. The laser weld bead was generated at the center of the overlapped region. Nitrogen gas at a pressure of 1 bar was also used to shield the welding. The details of this experimental setup and the properties of the laser are shown schematically in Fig. 1.

Detailed chemical compositions of both Al and Cu are shown in Table 1. The laser power and welding speed were varied to achieve the desired volume energy input for successful joining. To achieve successful welding, the welding parameters, such as laser power and welding speed, were varied depending on the total thickness of the workpiece. The laser power was varied between 500 and 900 W with an interval of 100 W, whereas the welding speed was varied between 10 and 45 mm/s with an interval of 5 mm/s, as shown in Table 2. Three different thicknesses of Cu, such as 0.5, 1, and 1.5 mm, were varied at the bottom, while the top sheet thickness of Al was kept constant at 0.5 mm. This typical experimental setup to join Al and Cu in three different configurations is shown schematically in Fig. 2a. The volume energy was calculated using Eq. 1, as shown below: [39]

$$E = \frac{P}{V \times A} \tag{1}$$

where in Eq. 1, E is used to represent volume energy (kJ/mm^3), P is denoted as laser power output (watt), A is used to describe the laser beam spot area (mm^2), and V represents the welding speed (mm/sec). Depending on the set of laser parameters, the volume energy varied, generating four different conditions of the weld: top sheet burnout, over weld, surface defect, successful welding, and no weld. The laser parameters were optimized to generate adequate volume energy for successful welding. The welds' mechanical, electrical, and material properties were analyzed. The post-weld experiments are also schematically displayed in Fig. 2b–e.

2.2 Mechanical and electrical properties analysis

The lap shear tensile test specimens were 80 mm in length and 10 mm in width (Fig. 2c). All the successful welds were subjected to uniaxial tensile loading at a uniform cross-head speed of 5 mm/s using the Shimadzu Ag-X, 250 kN-300 kN tensile testing machine. Since the bottom Cu sheet's thickness varied, the joint's total thickness was 1 mm, 1.5 mm, and 2 mm. Based on the breaking loads of all three configurations of welds, the welds with the highest breaking load were further selected for the in-detailed electrical resistance measurement and microhardness testing.
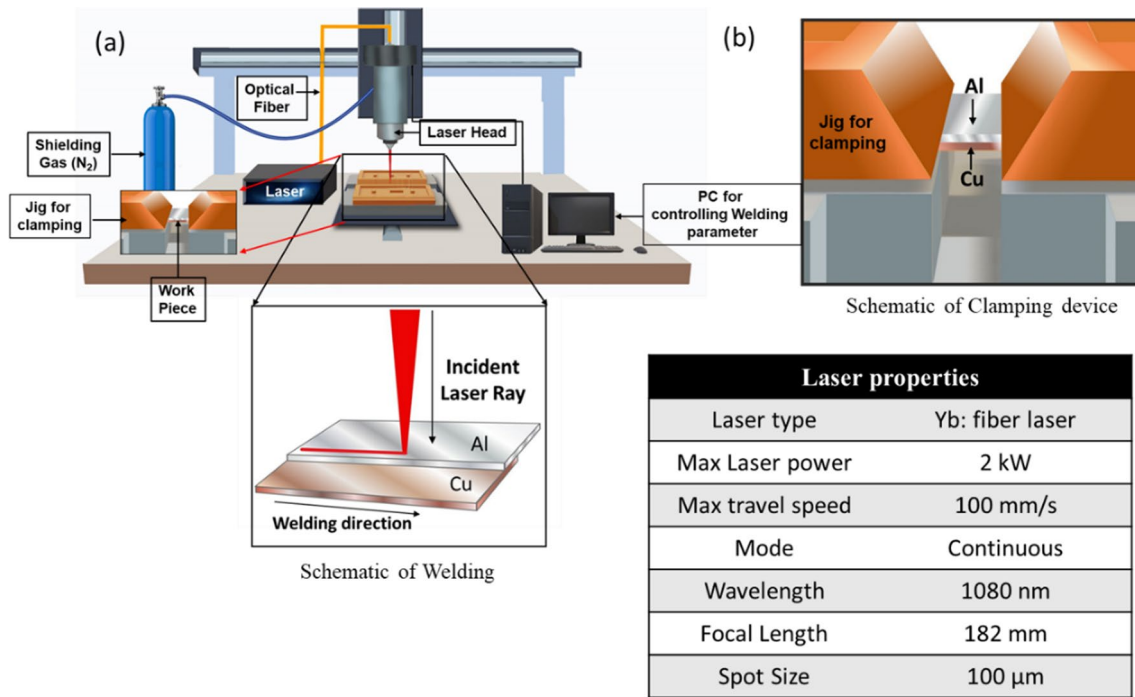
Fig. 1 Schematic of laser welding

Table 1 Al 1060 & Cu (UNS C10100) Chemical Composition

Elements (wt%)	Al	Cu	Si	Fe	Mn	Mg	Zn	Ti	Others
Aluminum (1060)	Bal	0.01	0.07	0.30	0.02	0.01	0.01	0.02	0.01
Copper (UNS C10100)	0.00	99.99	0	0	0	0	0	0	0.01

Table 2 Parameters experimented with

Aluminum thickness (mm)	Copper thickness (mm)	Laser power (W)	Welding speed (mm/s)
0.5	0.5	500–900	10–45
	1		
	1.5		

The Vickers microhardness on the cross sections of the three best breaking load conditions was carried along the two lines on the Al and Cu. A microhardness machine of the Mitutoyo HM-100 series was used to carry out this analysis. The horizontal line of hardness measurement on the Al was 0.15 mm from the joint interface. In the case of the copper side, the line was 0.16 mm from the interface. The hardness points were tested with a load of 0.49 N for a dwell time of 10 s, and the distance between each point was kept at 0.125 mm.

Electrical resistance across the joint was measured using a four-point resistance measurement system using a high-precision voltmeter made up of Keithley Integra Series Model 2460 ohmmeter [40, 41]. The current used for measurement was 100 mA which was applied for 60 s, and then, the average value of the four times measured resistance was considered. The specimens used for the electrical resistance measurements were precisely identical to the lap shear tensile testing. The detailed schematic diagram of the lap shear tensile testing for analyzing the breaking load of the joints and microhardness analysis at the cross sections of the joints are shown in Fig. 2b, c. Figure 2d also depicts the schematic diagram of the electrical resistance measurement process.

2.3 Microstructural analysis (SEM, EDS, and EBSD)

For each case of different bottom Cu sheet thickness, the combination of laser parameters that generated the highest breaking load was inspected in detail for the microstructural analysis. The cross sections were prepared perpendicular to the welding direction and were mounted and polished to produce a scratch-free surface for microstructural analysis. A standard metallographic grinding technique using MRE papers ranging from 320 to 1200 grit was applied for

Fig. 2 Schematics of welding and post-welding experiments. **a** Variation of bottom Cu sheet thickness. **b** Cross-section preparation for microstructural and microhardness. **c** Lap shear tensile test specimen specification for breaking load analysis. **d** Electrical resistance measurement process. **e** Lap shear tensile test process
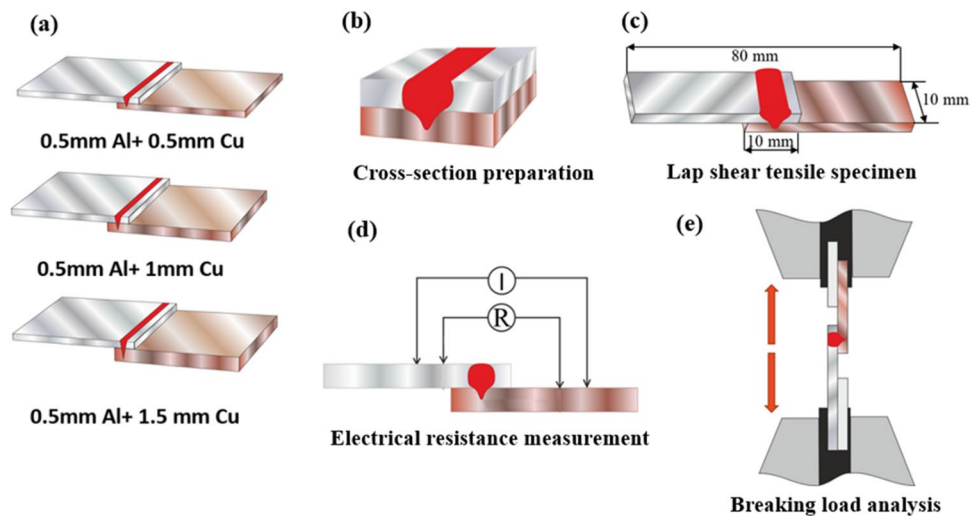
polishing. Furthermore, a glycol-based diamond paste of 1.0 μm and a colloidal of 0.4 μm were used to generate a scratch-free mirror-like surface for the EBSD and FE-SEM analyses. The SEM and EDS of the samples were carried out using Mira CMH, TESCAN, Brno, Czech Republic. The beam intensity was 20.0 kW, with a working distance of 15.3 mm. Line, area, and point analyses were carried out to find the formation of the intermetallic and see the material mixing phenomena. EBSD analysis was performed using Sigma 500 Fe-SEM made by Carl Zeiss using a detector of EDAX (TSL Hikari Super-model). The results were obtained by scanning the sample with a step size of 2.5 μm and grain tolerance angle of 10°. Two maps of inverse pole figure (IPF) and grain boundary character distribution (GBCD) were carried out to understand the grain structure and boundary characteristics. High-angle grain boundary (HAB) was fixed at angles higher than 15° (up to 180° measured). Furthermore, misorientations ranging between 2 and 15° were considered as low-angle grain boundaries (LAGB).

3 Results and discussion

3.1 Weld appearances

As shown in Table 2, laser parameters, such as the laser power and speed, were varied to carry out the welding successfully. In this work, the acceptable welding is generally considered as welds where no observable surface defects could be found. Based on Eq. 1, the volume energy for each set of parameters was calculated. Figure 3 depicts the schematic appearance of various welding conditions and original specimens concerning bottom Cu sheet thickness change and volume energy input. Furthermore, in Fig. 3a, we can see that in between the given range of volume energy input of 1.81–2.54, 2.18–3.18, and 5.73–7.64 kJ/mm^3, acceptable

welding could be observed for the bottom Cu sheet thickness of 0.5, 1, and 1.5 mm. Hence, it can be clearly observed from Fig. 3a that as the bottom plate thickness increases, acceptable welding could be achieved at a higher and broader range of energy input. The energy input for welding thicker sheets, when applied for joining less thick plates, the welds resulted in a lower breaking load. It is expected that the energy input, which is adequate for the higher thickness of the bottom Cu sheet, results in excess heating for thinner sheets and induces the excessive formation of brittle microstructure and softening. Furthermore, it was also noticed that as the bottom Cu sheet thickness was increased to 1.5 mm, the energy input applied for thinner sheets also resulted in a weak joining. Hence, it is predicted the energy input, which was adequate for thinner bottom Cu sheet thickness, generates insufficient penetration for thicker bottom Cu sheets. Below the 1.81 kJ/mm^3 volume energy input, only the formation of the weld bead took place on the aluminum plates, whereas no joining could be observed as the weld bead did not touch the copper surface. Any energy input above 7.64 kJ/mm^3 generated significant weld defects.

The type of defects varied depending on the increase in the volume of energy input. The highest amount of energy input went between 9.6 and 12.1 kJ/mm^3, resulting in top sheet burnout that generated partial joining or sticking of Al on the Cu surface. Over-welding was observed within the range of 8.1–9.2 kJ/mm^3 volume energy input, where the top aluminum sheet penetrated through the bottom copper sheet. Although these joints might appear to generate better strength, but they exhibited low strength due to excess energy input and penetration depth facilitating the formation of a high amount of brittle IMC, weakening the strength of the joint. Surface defects were generated within the energy input range of 7.3–8.1 kJ/mm^3, where the weld surface exhibited the formation of voids and discontinuity. Although this kind of defect does not pose any severe threat,

Fig. 3 **a** Various appearances of the welds at different volume energy inputs. **b** Variation of volume energy input for different thickness fractions in case of acceptable welds
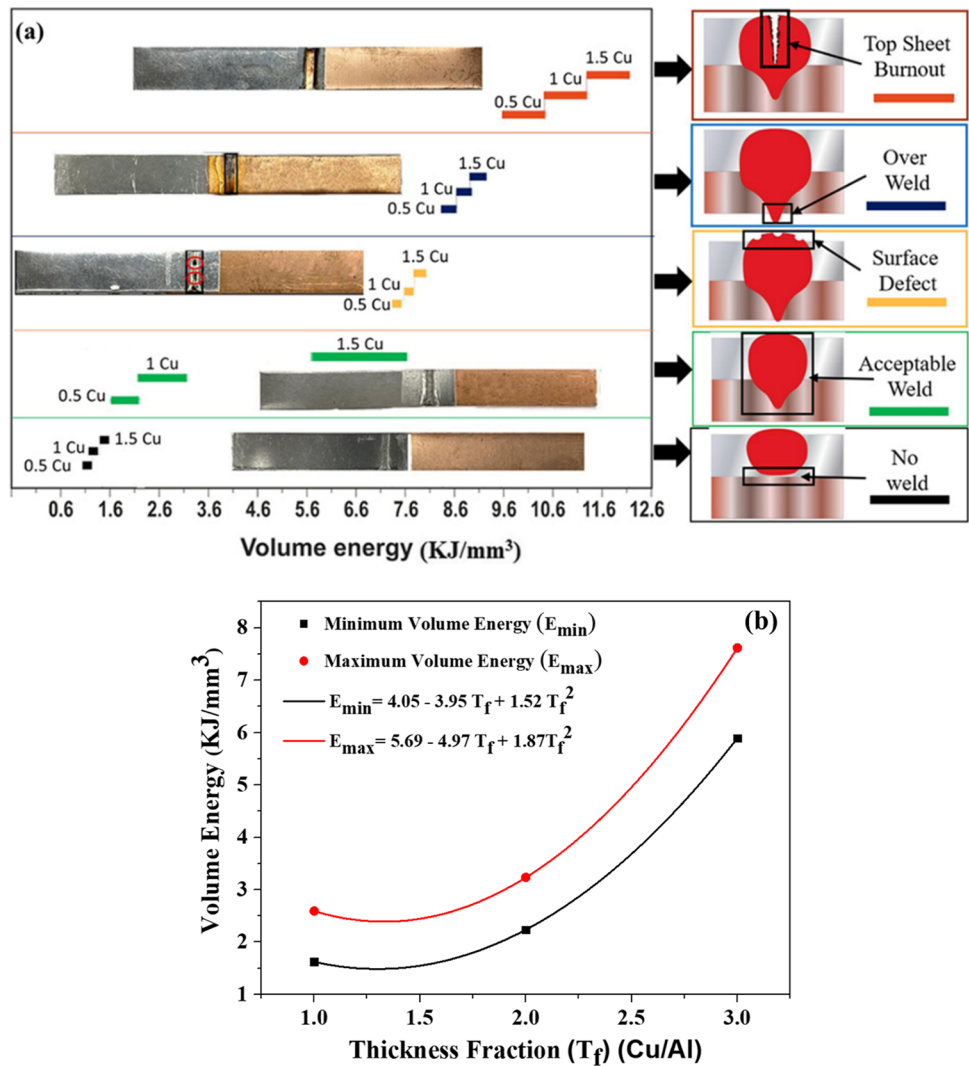
it is still better to avoid it. In laser welds, porosity can be formed due to numerous reasons such as keyhole instability, vortex molten metal movement, and hydrogen entrapment. The abovementioned conditions generally generate bubbles inside the molten metal during welding. During solidification, it may not release those back into the atmosphere, forming a pore on the surface. The surface appearances of this type of welding also suggest that these types of porous structures may be present deep inside the welds and can deteriorate the electrical and mechanical properties [42–45] [46–49].

To observe changes in the maximum and minimum volume laser energy input for acceptable welding by increasing the bottom Cu sheet thickness, a graph was plotted between abovementioned two entities, as shown in Fig. 3b. The x-axis represents the thickness fraction (T_f), which is the ratio of copper and aluminum plate thicknesses. To represent the thickness fraction as a whole number, the thickness of the copper plate was used as a numerator. Figure 3b shows that

as the thickness fraction increases, the range between which acceptable welding can be achieved also increases. Additionally, the maximum and minimum volume energy input increases with an increase in the bottom Cu sheet thickness. It appears that the trend in the increase of both maximum and minimum required volume energy to be a polynomial function where a term of square of thickness fraction (T_f) exists. The indetailed equation of the E_{max} and E_{min} is stated inside the graph. However, this work only considers three cases of thickness fraction variation in welding. Thus, this trend may change if the thickness fraction value is changed below 1 and above 3.

3.2 Breaking load of the joints

All the successful joints obtained within the energy input variation of 1.81–7.64 kJ/mm³ for all three types of the thickness of the bottom copper sheet were tested with lap shear tensile tests. The breaking loads and the associated

laser parameters for 0.5-, 1-, and 1.5-mm thick bottom copper sheets are tabulated in Tables 3, 4, and 5. For each laser power shown in these tables, weld speeds varying from 10 to 45 mm/s by varying 5 mm/s were applied. But the combination of parameters other than those shown in the Tables 3, 4, and 5 either generated welding defects or their breaking load is below 150 N. Four sets of energy inputs were identified for each type of bottom Cu sheet cumulating to 12 sets of energy input, generating a breaking load above 150 N. For further discussion of the weld properties such as electric resistance, weld bead width, and depth of penetration, these 12 sets will be used only. Specimens with the highest breaking load for 0.5-, 1-, and 1.5-mm bottom Cu sheet were graphically represented in Fig. 4a by breaking load versus displacement graph. The data tabulated in Tables 3, 4, and 5 and the breaking load graph represented in Fig. 4a suggest that the highest possible breaking load could be achieved for a 1.5-mm thick bottom copper sheet joint, which is 373.95 N. The highest possible breaking loads achieved for bottom Cu

sheet thickness of 0.5 and 1 mm were 244.02 N and 313.56 N, respectively. The volume energy input versus breaking load graph shown in Fig. 4b for all three cases of the bottom Cu sheet depicts that as the bottom Cu sheet thickness was increased, the volume energy input for weld increased. Furthermore, as the welds could be carried at higher energy input values, the breaking load also increased remarkably.

The highest possible breaking loads for each type of bottom Cu sheet thickness are marked by the circle and are connected by a line to show a trend. This trend is interesting: the second highest volume energy input always generated the highest possible breaking load for all three cases. It is also observed from Fig. 4b that irrespective of any bottom Cu sheet thickness, the breaking load increases gradually as the energy input is increased to second highest value. After that, it decreases sharply. Hence, the combination of laser parameters that generate adequate energy input resulting in the highest possible breaking load for a specific bottom Cu sheet thickness can be designated as optimized laser welding

Table 3 0.5 Al + 0.5 Cu

Laser input		Weld properties				
Laser power (W)	Weld speed (mm/s)	Volume energy (J/mm^3)	Bead width (mm)	Depth of penetration (mm)	Resistance (mΩ)	Breaking load (N)
500	25	2547.77	1.35	0.12	0.15	200.271
	35	1819.83	1.30	0.11	0.16	156.482
600	30	2547.77	1.25	0.13	0.17	213.384
700	35	2548.23	1.15	0.15	0.18	220.894
	40	2229.29	1.17	0.14	0.17	198.179
800	40	2547.77	1.18	0.16	0.19	211.477
	45	2266.28	1.20	0.18	0.18	244.021

Table 4 0.5 Al + 1 Cu

Laser input		Weld properties			
Laser power (W)	Weld speed (mm/s)	Bead width (mm)	Depth of penetration (mm)	Resistance (mΩ)	Breaking load (N)
500	20	1.22	0.19	0.34	279.390
600	35	1.18	0.21	0.33	248.910
700	35	1.17	0.32	0.34	240.52
800	35	1.16	0.42	0.31	313.56

Table 5 0.5 Al + 1.5 Cu

Laser input		Weld properties			
Laser power (W)	Weld speed (mm/s)	Bead width (mm)	Depth of penetration (mm)	Resistance (mΩ)	Breaking load (N)
900	15	1.16	0.54	0.12	259.637
800	15	1.10	0.67	0.14	373.959
700	15	1.14	0.61	0.13	267.563
600	10	1.12	0.64	0.14	285.575

Fig. 4 **a** Breaking load versus displacement. **b** Breaking load versus volume energy graph. **c** Breaking load versus thickness fraction for 0.5-, 1-, and 1.5-mm bottom Cu sheet thickness

3.3 Depth of penetration and weld bead width variation

The weld penetration depth and weld bead width showed a similar trend when the volume energy input was increased gradually, as depicted in Fig. 5a, c. Our earlier discussion pointed out that the optimized energy input increased as the bottom Cu sheet thickness increased, resulting in an increase in breaking load due to increased penetration depth. Hence, to justify this claim particularly, the cross sections of the successful welds were cut, and the penetration depth was measured under the SEM. The finding proves the previous claims, as shown in Fig. 4a, b. The top of the weld bead was also measured, and its value was demonstrated graphically in Fig. 5c. The observed trend depicts; as the energy input

parameters. Thus, any energy input both below and above optimized volume energy will inevitably reduce the breaking load of the joints. It is speculated that the optimized set of laser parameters generated adequate penetration depth and contact area and facilitated the evolution of IMC phases required for the best possible breaking load for weld properties. The highest possible breaking load for each type of bottom Cu sheet thickness versus the sheet thickness fraction of the Cu/Al graph has been shown in Fig. 4c. Figure 4c revealed a trend of linear increase of breaking load with an increase in thickness fraction with a positive slope value of 64.97 and R^2 value of 0.99.

increased, the weld bead width increased gradually for all three types of bottom Cu sheet thickness. However, from both Fig. 5c and d, it could be identified that as the bottom Cu sheet thickness was increased the weld bead width decreased. The reduction of the weld bead with increasing the heat input and bottom Cu sheet thickness can be justified by the fact that when a material with higher thermal conductivity, such as copper [50], is kept at the bottom, it is expected that the tendency of heat flowing downward will be higher than in the sideways. In Fig. 5b, d, the trend of gradual decrease of weld bead width and increase of penetration depth with increasing thickness fraction has been shown. The penetration depth increased with a positive slope of 0.235, whereas the weld bead decreased with a negative slope of 0.06, and their respective R^2 values are 0.99 and 0.98. For both the graphs in Fig. 5b, d, the weld penetration depth and weld bead width's value were taken from the circled values as shown in Fig. 5a, c. The circled values belong to those welds generated by applying the same weld parameters which generated high breaking loads.

3.4 Weld cross-section observation and mode of welding influencing material flow

The SEM of the cross sections of the joints with the highest penetration depth generating high breaking load and low electrical conductivity for each case of bottom Cu sheet thickness of 0.5, 1, and 1.5 mm is shown in Fig. 6a–c.

Fig. 5 **a** Depth of penetration variation versus volume energy input. **b** Depth of penetration variation trend with increase in thickness fraction increase. **c** Weld bead width variation versus volume energy input. **d** Weld bead width variation trend with increase in thickness fraction increase
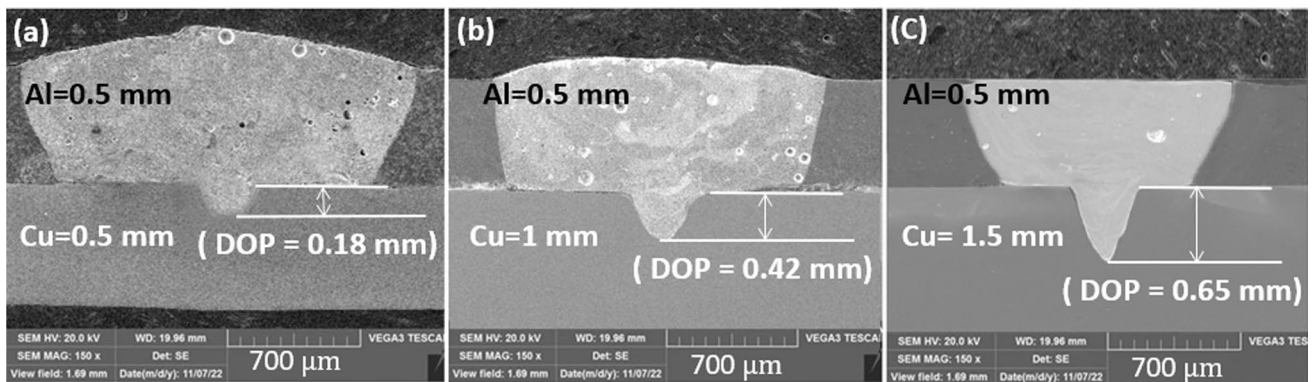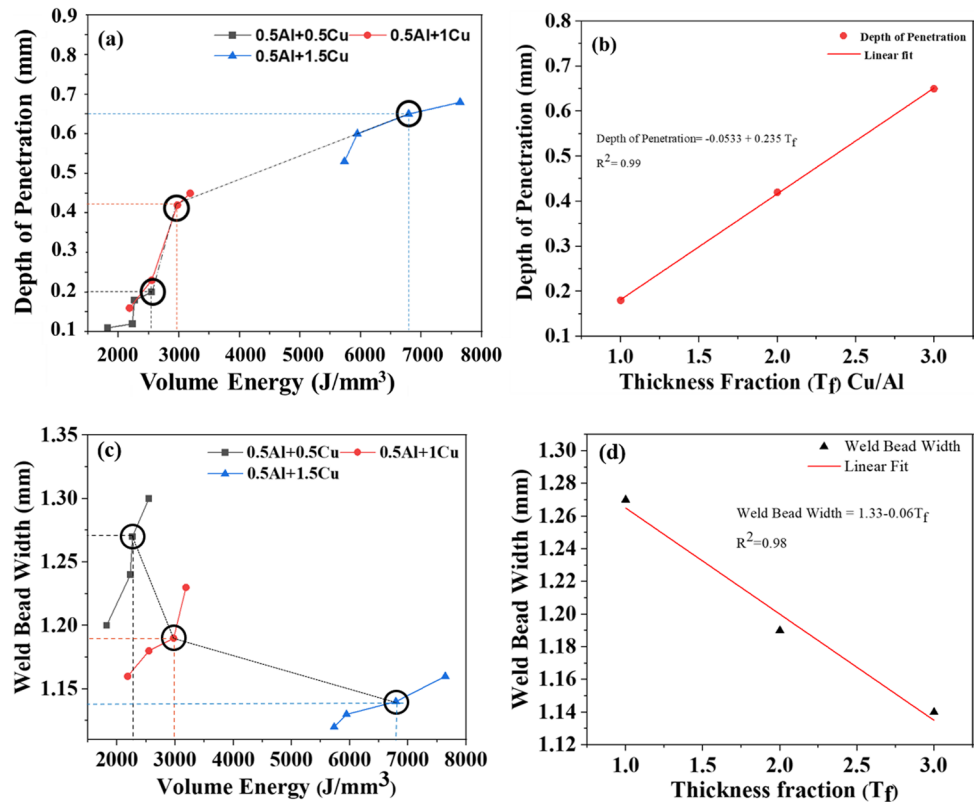
Fig. 6 SEM of weld cross sections **a** 0.5-mm, **b** 1-mm, **c** 1.5-mm bottom Cu sheet

The earlier graphical representation of the data and the cross-sectional images jointly depicted that by increasing the bottom Cu sheet thickness, the penetration depth could be increased successfully so that the strength of the joining is not hampered. Although no significant defect size could be observed for all three cases, some porosity might still be present at a microscopic level. These defects are expected not to affect the mechanical properties of the welds significantly.

As the weld cross section suggested, the penetration depth was minimal for a 0.5-mm bottom Cu sheet as the possibility to apply high energy was less. Hence, the welding was carried out mostly in conduction mode. Figure 7a, b shows the copper and aluminum distribution in the weld penetration zone. Inside the penetrated region, the presence of Al is predominant, whereas the amount of copper is less. The top sheet melts entirely in the conduction welding mode, whereas the lower sheet melting is restricted. Furthermore, due to less energy input and low melting, no vapor is generated, which also lowers the recoil pressure. Thus, the formation of vortex flows and intermixing of metals is much lower inside the weld pool. Due to the combined effect of all the phenomena mentioned above, only a few copper layers are observed, mostly due to the melted Cu and Al mixture. In addition, the diffusion of

solid copper from the unmelted zone is extremely low due to lower energy input.

The Al and Cu EDS area mapping for a 1-mm thick bottom Cu sheet is shown in Fig. 8a, b. Compared to 0.5-mm thick bottom Cu sheet weld, high penetration depth could be achieved as the welding took place at a higher energy input. Due to the application of higher energy input, it is estimated that the welding has occurred in a combination of conduction and keyhole mode. A clear indication of Cu entering even inside the top of aluminum could be seen in the middle portion of the Cu map. Furthermore, inside the Cu map, the vortex flow could be easily understood as a small vortex could be seen at the bottom right corner. Hence, the observed phenomenons indicated a greater extent of mixing inside the weld has occurred between Al and Cu. It is estimated that the metal vapor generated and the dissimilar viscosity at elevated temperatures favored the vortex flows and enhanced material mixing. Since the welding was carried out at higher energy levels, diffusion of unmelted Cu could also occur, which results in the enrichment of Cu quantity inside the weld.

In Fig. 9a, b, the EDS map for Al and Cu is shown for the 1.5-mm thick bottom Cu sheet welding. The SEM images in Figs. 6c and 9a, b exhibit the weld being carried out in pure conduction mode. From the earlier results, it has been observed that this welding was carried out at the highest possible energy input values. Inside the weld, a huge accumulation of the Cu has been observed. Although no clear indication of the vortex flow could be seen, it is anticipated that due to the huge amount of Cu incorporation, the trace of the vortex was hard to find due to the diffusion and melted material intermixing. In contrast, in the SEM image of Fig. 6c, some hints of light and darker regions could be observed, further indicating the formation of the vortex flow inside the weld. Hence, it can be understood that variation in energy input due to the change in bottom sheet thickness also alters the welding mode. The three modes of welding, pure conduction, conduction and keyhole, and pure keyhole, are
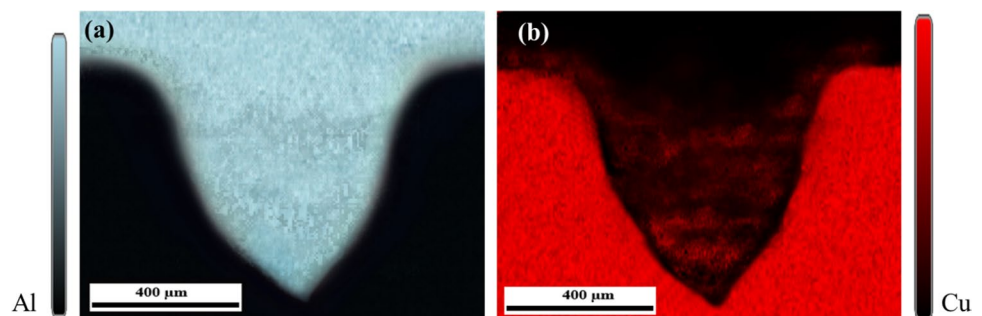

Fig. 7 EDS map of **a** Al and **b** Cu for 0.5 Cu bottom sheet
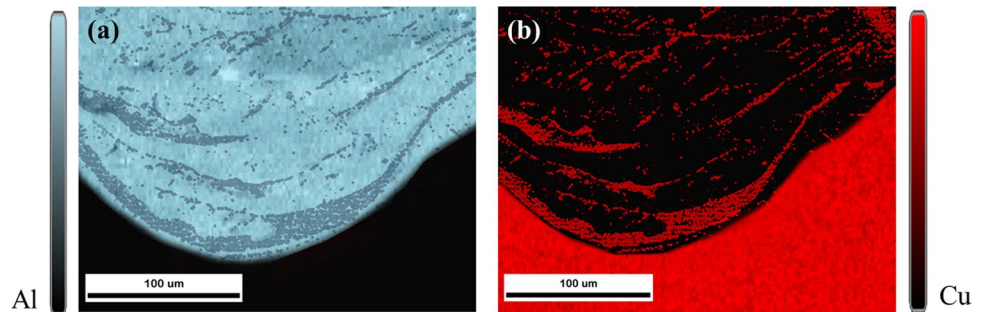
Fig. 8 EDS map of **a** Al and **b** Cu for 1.0 Cu bottom sheet
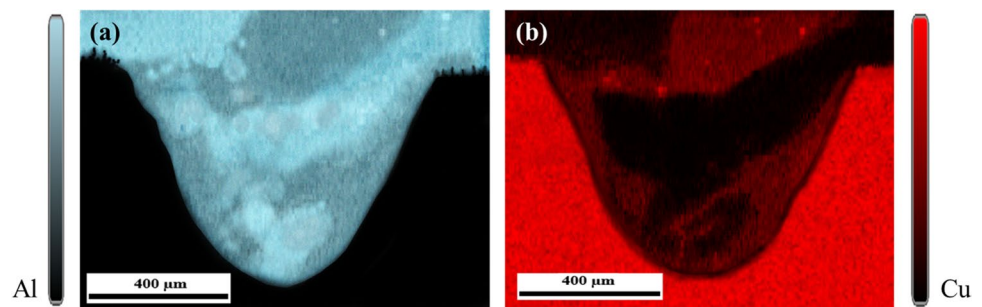
Fig. 9 EDS map of **a** Al and **b** Cu for 1.5 Cu bottom sheet

also schematically expressed in Fig. 10a–c. In Fig. 10a–c, we can clearly see that in conduction welding the achieved depth of penetration is less, whereas it is highest in case of pure keyhole. Hence, it can also be suggested that for thin sheets conduction mode welding is appropriate whereas for thicker sheets keyhole is preferred. The earlier results from voume energy input versus thickness fraction also supports the similar suggestion [51–54].

3.5 In-detailed microstructural characterization

3.5.1 SEM and EDS

The joining mechanism during the welding of aluminum and copper plays a vital role in understanding the resulting properties of the weld. From Fig. 4b, a clear idea of which welded joint generated the best possible breaking load for a particular thickness of bottom sheet copper can be obtained and marked carefully. Hence, microstructural characterization of the best welding for three categories was done to justify the observed fact that increasing the bottom Cu sheet thickness facilitates high mechanical strength. SEM images of those best welds are shown in Fig. 6a–c. In Fig. 6, we can find that the images were taken at a magnification of ×150 and show no notable defects, such as large cracks and porosity. During the welding process, the bead was mostly generated over aluminum, and the molten aluminum penetrated inside the copper surfaces and formed a joining which is also confirmed by Figs. 7, 8, and 9. The depth of penetration (DOP) achieved for 0.5 mm Cu was 0.18 mm; for 1-mm

thick Cu, the DOP was 0.42 mm; for 1.5 mm of Cu, the DOP was 0.65 mm. The aluminum weld area is more than Cu for all the welds, and it bulges outwards. Aluminum has a higher expansion coefficient than copper. Hence, when melted by laser irradiation, it spreads more on the copper surface and produces a larger contact area at the joining interface. High-magnified SEM images and their EDS analysis were carried out to study in detail and check the joint interface.

In-depth SEM and EDS area, line, and point analysis were carried out at the Al-Cu interface and are shown in Fig. 11. The SEM, in Fig. 11a, clearly shows the penetration of Al inside the Cu for which there will be diffusion of Cu inside the penetrated Al. The EDS line, point, and area analysis was carried out on the region (i) of Fig. 11a, which is shown in Fig.11b at a magnification of ×1400. The results of the area scanning, as shown in Fig. 11c, d, and f, clearly show the Cu entering the Al region. The same phenomena can also be made by line and point analysis as the Cu concentration growing inside the Al can be seen in Fig. 11e and the table indicating the atomic percentages of Al and Cu. The point analysis inside the Al and Cu region was carried out to check the formation of the IMC. The point analysis near the Al-Cu interface points 2 and 3 exhibits the appearance of Al-rich Al_2Cu and AlCu intermetallic with some unreacted Al. Point 1, which lies a little far from the interface, also revealed the formation of AlCu with some unreacted Al. The point 4 measurement showed 99% Cu concentration, confirming no diffusion from the Al side towards Cu. Since the welding was carried out at a higher temperature above the melting point of the Al, diffusion of the copper atoms

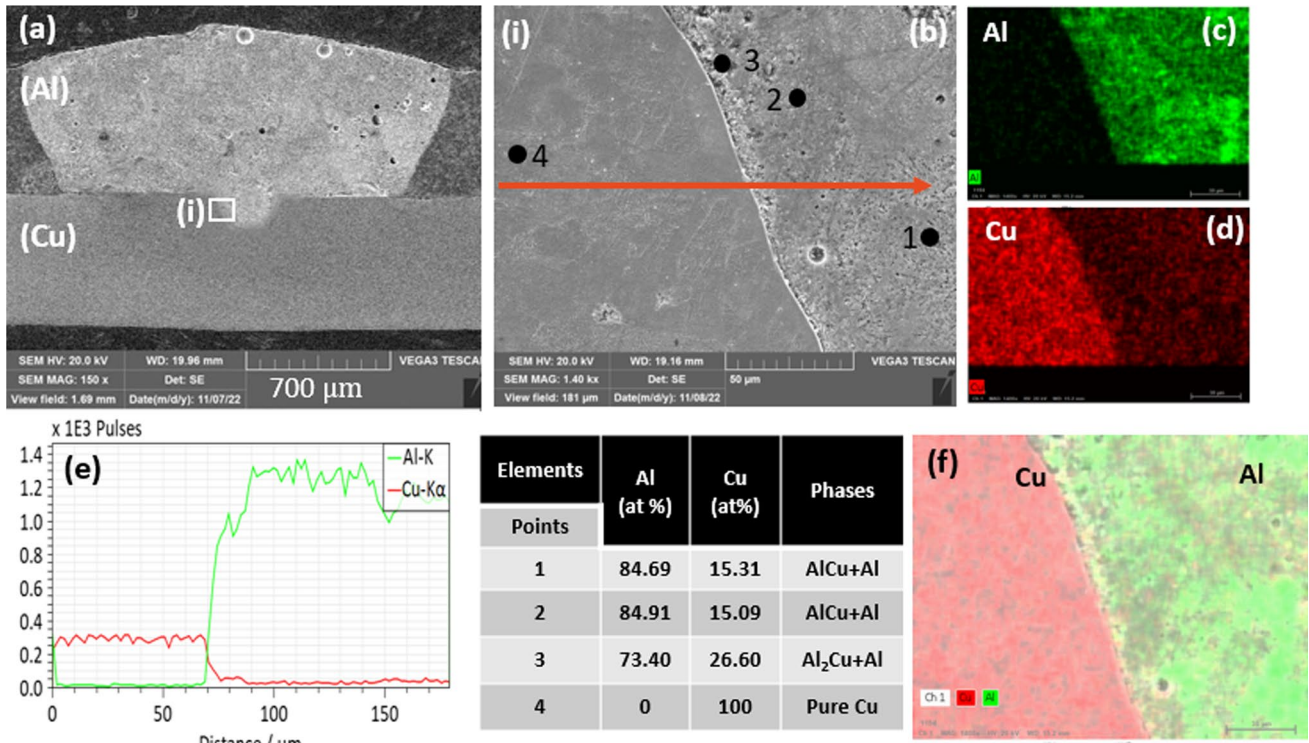**Fig. 10** **a–c** Schematic diagram of various modes

(a) Conduction mode (0.5+0.5)

(b)Conduction + Keyhole mode (0.5+1.5)

(c) Keyhole mode (0.5+1.5)
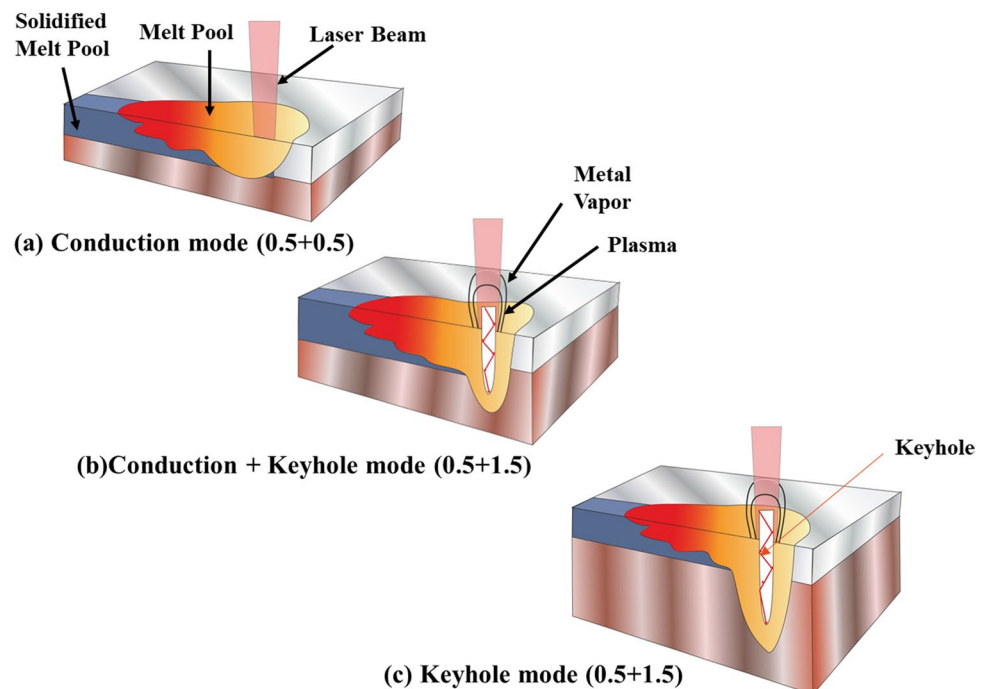
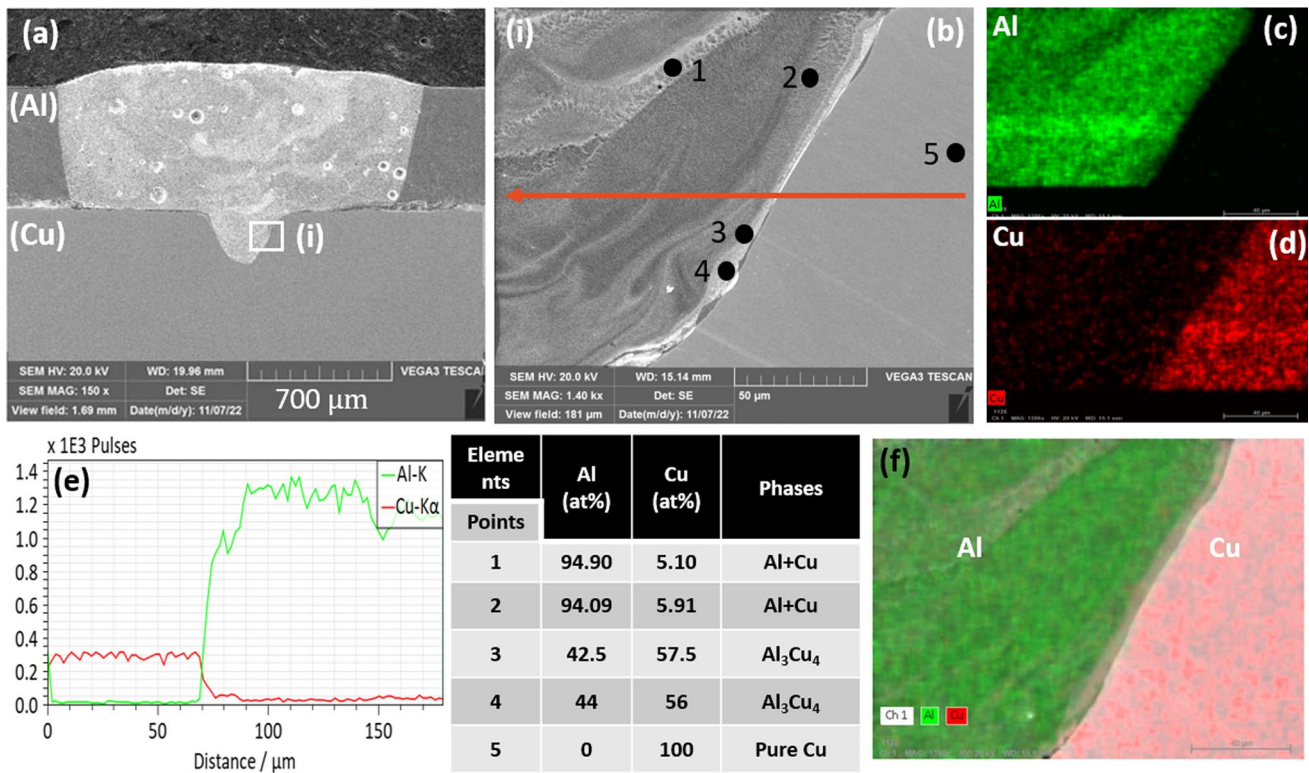**Fig. 11** In-depth SEM and EDS for 0.5-mm thick Cu bottom sheet

Fig. 12 In-depth SEM and EDS for 1-mm thick Cu bottom sheet

took place, which caused the evolution of IMC inside the weld [55]. Furthermore, as almost all of the point analyses exhibited Al-rich IMCs, the diffusion of Cu inside the Al was low. From our earlier discussion, it was observed that the welding for the 0.5-mm bottom Cu sheet was carried out at a lower volume energy input. Hence, it is evident that the diffusion of Cu inside the Al for lower energy input will be less. Although in the material joining process, there are instances where diffusion from the Al side has taken place towards copper during Al-Cu joining. However, that chance is low in laser welding as the process is fast, and rapid solidification occurs, ceasing further diffusion.

A similar type of SEM and EDS analyses was carried out for the weldment of the bottom Cu sheet thickness of 1 mm, as shown in Fig. 12. The magnified view of region (i) of Fig. 12a is shown in Fig. 12b. The region (i) was ×1400 magnified; thus, it revealed some new morphology forming inside the weld. Some white layers mixing with the dark layer can be seen, which hints at the formation of new types of phases compared to the bottom Cu sheet thickness of 0.5-mm welding. As shown in Fig. 12e, the line scan result also depicted more Cu diffusing inside the Al than in the previous case. The EDS area scanning in Fig. 12c, d, and f also confirmed that, especially in white areas, the concentration of the Cu atoms is higher. Overall, four points inside Al and one point on Cu were measured to check the exact composition of those regions. Inside the white zones, i.e., on points 3 and 4, 57.5% and 56% of Cu concentrations were found. As a result, in points 3 and 4, Cu-rich IMC of Al_3Cu_4 was formed. On points 1 and 2 in the darker region, the Cu concentration was only around 6%, facilitating only the mixed mode of Al and Cu structure [56]. Like the previous case, point 5 shows 100% Cu concentration indicating no diffusion from the Al side to Cu. Since welding was performed on the bottom Cu plate thickness of 1 mm using a higher volume energy input, a greater quantity of Cu diffused inside the weld, forming Cu-rich IMC. In addition, since it is observed that Cu diffusion is higher in this case, the chances of developing other IMC, such as Al_2Cu and AlCu, are also high. The Cu-rich IMCs possess higher hardness values, whereas the Al-rich ones have less hardness. Hence, inside the weld, a mixture of hard and softer IMC is expected to enhance the mechanical performance of the joint. This result correlates well with the previously observed breaking load versus energy input results [57].

The SEM and EDS analyses for welding the bottom Cu sheet thickness of 1.5 mm are shown in Fig. 13. ×4000 magnified SEM result of the region (i) of Fig. 13a revealed the formation of entirely different morphological structures, as shown in Fig. 13b. The morphological appearances hinted at the formation of a mixture of Al-Cu eutectic structures and the columnar dendrites inside the weld. The EDS line and area mapping in Fig. 13c, d, e, and f typically showed a very high amount of Cu diffusion inside the weld. Especially in line scanning, some regions showed almost overlapping concentrations of both Al and Cu which mostly indicates the formation of the Al-Cu eutectic mixture. Since this concentration coincided almost at the end of the line, it is speculated that the eutectic structures mostly form at the lower center of the welding. Fine columnar intermetallic structures can be seen growing at the interface region where the copper concentrations were high. At points 1 and 2, where Cu and Al concentrations were 36.68 and 63.32% and 39.43 and 60.57%, respectively, the formation of the mixture of Al_2Cu and Al and the mixture of Al_2Cu and Cu could be occurring. High copper concentrations of 68.49% and 69% were observed at points 3 and 4, respectively, near the interface, indicating the formation of Al_4Cu_9 IMC phases [58, 59]. Since the welding for this case was done at the highest possible volume energy input, it is quite natural that the amount of Cu diffusion is the highest. The welded region revealed numerous soft and brittle Al-rich and Cu-rich IMC mixtures. It is speculated that the formation of mixtures of hard and comparatively softer phases enhanced the mechanical properties of the joint, and it also correlates well with the observed highest possible breaking load results.

3.5.2 EBSD analysis

The EBSD analysis for 0.5-mm thick bottom Cu sheet welding is shown in Fig. 14a, b, where Fig. 14a represents the inverse pole figure (IPF) and Fig. 14b represents the grain boundary characteristic distribution (GBCD) map. We previously discussed that the interface region between Al and Cu exhibited a higher percentage of IMC phases and changes in elemental distribution, which were caused by Cu diffusing into the Al penetrating the Cu. The IMC characteristics and elemental distribution in dissimilar metal welding contribute more to the final properties. Since the Cu diffusion chances and formation of IMC are higher in the region, it was further chosen to observe the characteristics of the grain and the grain boundaries. The IPF in Fig. 14a depicts the formation of an elongated grain structure inside the Al penetrating the copper. However, the grains are finer and equiaxed inside the Cu base material. It is quite interesting to note that the grain structure at the interface exhibits very fine structures, which are even finer than those of the base Cu material. Furthermore, its morphology is different from the other elongated Al grain structures. Additionally, such kind of grain structures can also be observed inside the Al penetrating the Cu region, albeit in smaller quantities. In the GBCD map of the same region, we find that high-angle grain boundaries (HAGB) formed mostly inside the weld. Interestingly, the concentration of HAGB is also significantly higher in areas where finer grain structures can be seen. The Al penetrating inside the Cu is a solidified structure,
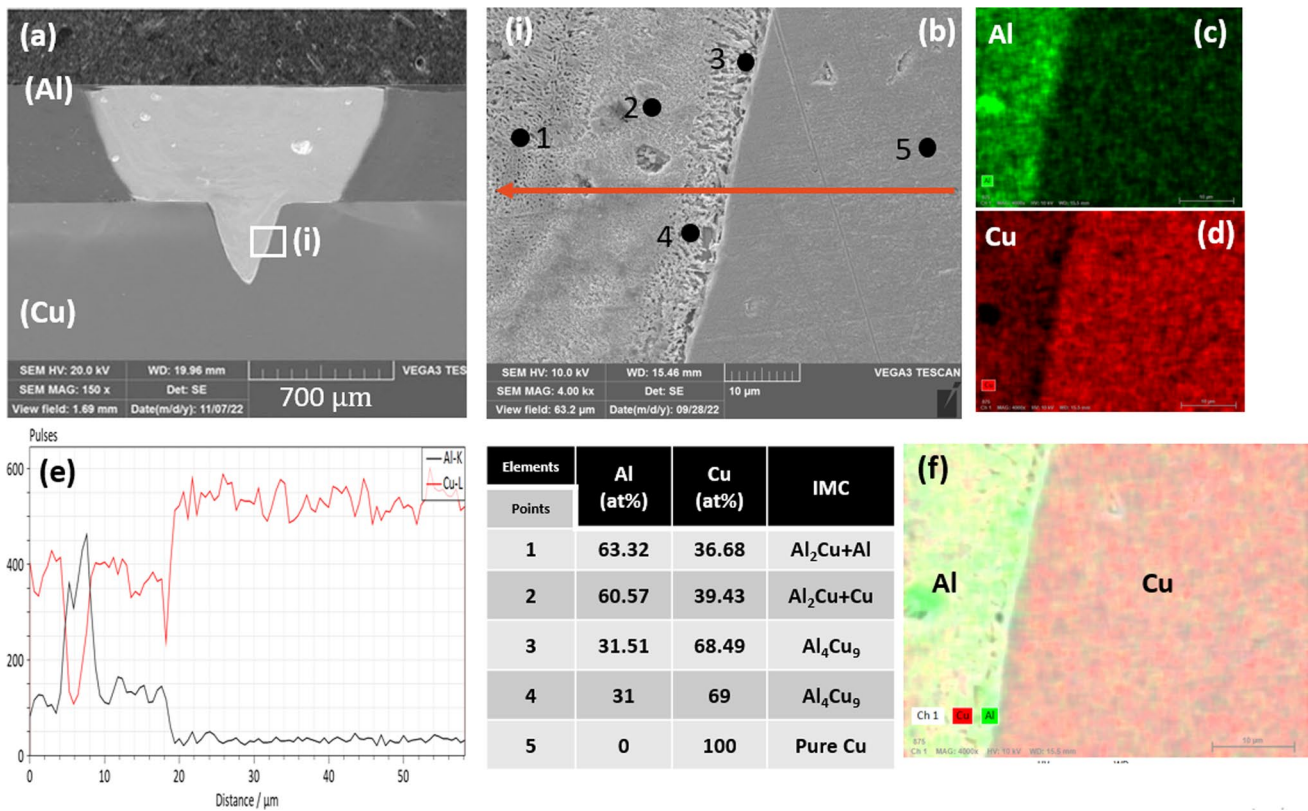
Fig. 13 In-depth SEM and EDS for 1.5-mm thick Cu bottom sheet

Fig. 14 EBSD analysis for 0.5-mm thick Cu bottom sheet. **a** Inverse pole figure (IPF). **b** Grain boundary characteristic distribution (GBCD)
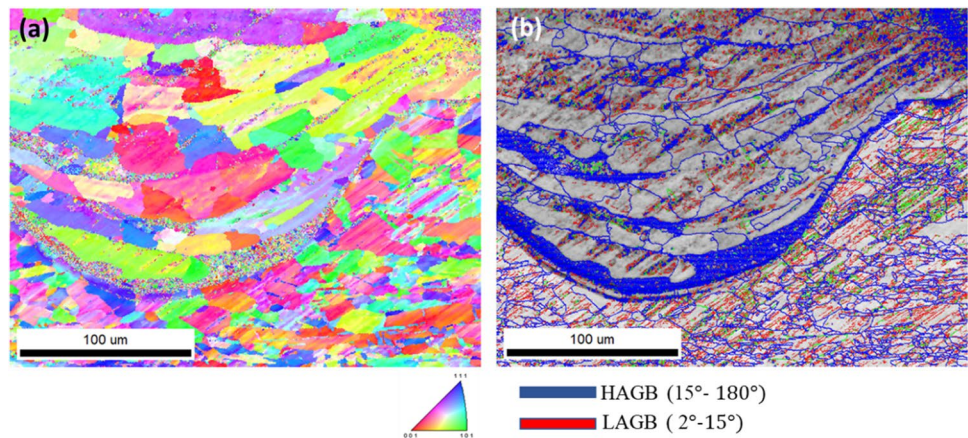

and its appearance confirms that the molten Al's cooling has taken place in all directions as the base copper material surrounds the molten pool. Generating the finer structure and higher concentration of HAGB at the interface of Al-Cu and even inside the weld ensures the formation of IMCs in those regions during the welding process. The IMC with high hardness contains higher concentrations of misorientations, and the degree of misorientations is also high. Hence, an area enriched with IMC will exhibit very fine structures with higher concentrations of HAGB [60, 61]. Interestingly,

in SEM and EDS analyses, we found that, for 0.5-mm thick bottom Cu sheet welding, a higher amount of IMC formed at the Al-Cu interface. Hence, the EBSD and the SEM/EDS analysis correlated well in analyzing Cu diffusion and melted copper mixing inside Al and creating Al-Cu IMCs.

In Fig. 15a, b, the EBSD analysis for 1-mm thick bottom Cu sheet welding is shown where Fig. 15a represents the IPF and Fig. 15b represents the GBCD map. Inside the Al penetrating Cu structure, the grains appear to be nearly equiaxed. The base Cu material exhibits a finer equiaxed structure like

Fig. 15 EBSD analysis for
1-mm thick Cu bottom sheet.
a Inverse pole figure (IPF). **b**
Grain boundary characteristic
distribution (GBCD)

Fig. 15 EBSD analysis for 1-mm thick Cu bottom sheet. **a** Inverse pole figure (IPF). **b** Grain boundary characteristic distribution (GBCD)
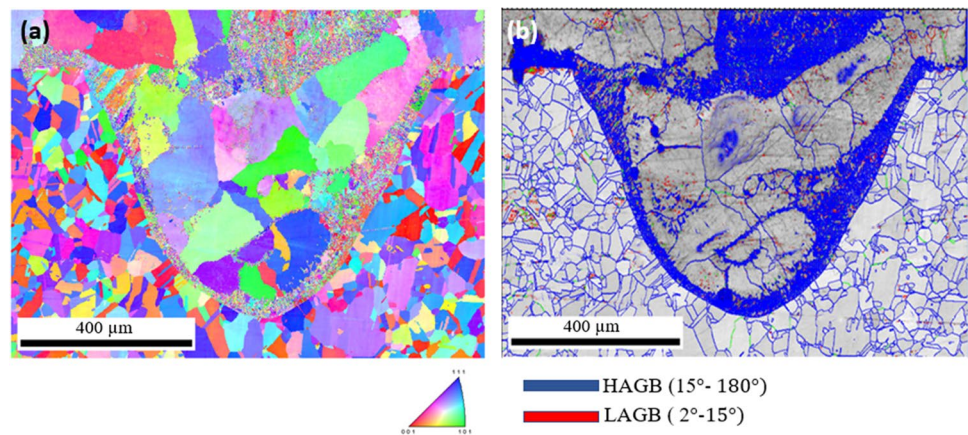
the earlier discussion. However, the area of the finer structures inside the same Al has increased remarkably. Similar observations can also be made in the GBCD map, where the area of HAGB is noticeably increased. The 1-mm thick Cu bottom sheet welding was carried out at higher heat input. Thus, it facilitates more diffusion of the Cu atoms inside Al and forms thicker zones of IMCs containing a higher amount of the HAGB, which enhances their hardness. This observation also confirms the findings from the SEM and EDS analyses conducted in this particular case. It explains why welding with a thicker bottom sheet and increased energy input could achieve a higher breaking load.

The IPF and GBCD for a 1.5-mm thick bottom sheet of Cu, as shown in Fig. 16a, b, depict the formation of very fine structures inside the Al penetrating inside the base metal Cu. Although the grain structure inside the base Cu remains similar, it changes remarkably inside the Al. This change can be easily distinguished as a huge amount of HAGB clustering occurred. The finer grain formation can also be noticed compared to the other two cases. The elongation of the grains inside the Al was remarkably lower. As discussed in the earlier two cases, IMC possesses a high quantity of misorientations with a high degree for which it contains a

very high amount of HAGB. Since the welding for a 1.5-mm thick Cu bottom sheet was carried out at the highest energy input, it facilitated the excess amount of Cu diffusion. When solidifying during cooling, this diffused Cu in the presence of Al transforms into IMC layers. The amount of IMC forming in this case, as seen in the EBSD maps and measured by EDS analysis, correlates well with the highest breaking load achieved for a 1.5-mm thick Cu bottom sheet with the highest possible energy input.

3.6 Microhardness analysis

Vicker's microhardness analysis was carried out on both Al and Cu side, and their respective hardness is shown in Fig. 17a, b. The hardness was measured along the lines as schematically shown in the insets of the figure. For both materials, the hardness inside the welded region went remarkably high. The highest increase in hardness was observed in the top sheet aluminum when welded with a 1.5-mm thick bottom Cu sheet, reaching almost seven times the strength of the base materials at approximately 350 Hv. The lowest value was nearly 200 Hv for joining a 0.5-mm thick bottom Cu sheet. For a 1-mm thick bottom Cu sheet,

Fig. 16 EBSD analysis for
1.5-mm thick Cu bottom sheet.
a Inverse pole figure (IPF). **b**
Grain boundary characteristic
distribution (GBCD)

Fig. 16 EBSD analysis for 1.5-mm thick Cu bottom sheet. **a** Inverse pole figure (IPF). **b** Grain boundary characteristic distribution (GBCD)
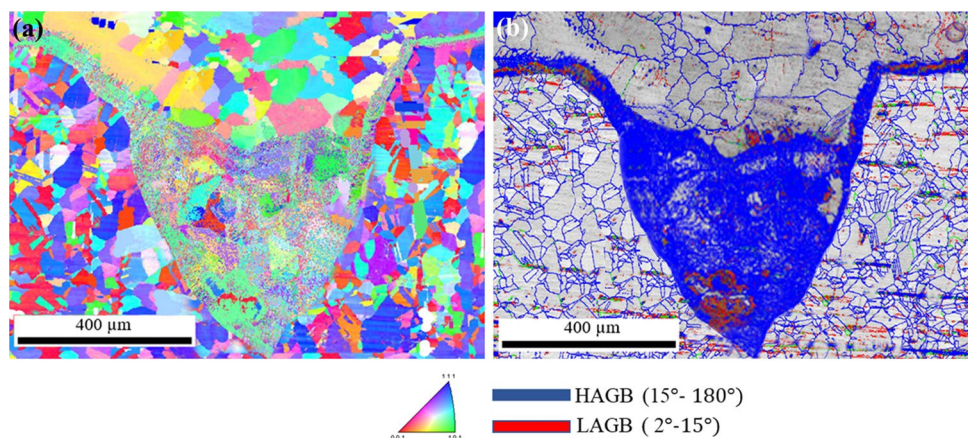
Fig. 17 Vicker's microhardness analysis. **a** Inside the top sheet aluminum. **b** Inside the base material Cu and Al penetrating Cu inside the bottom sheet
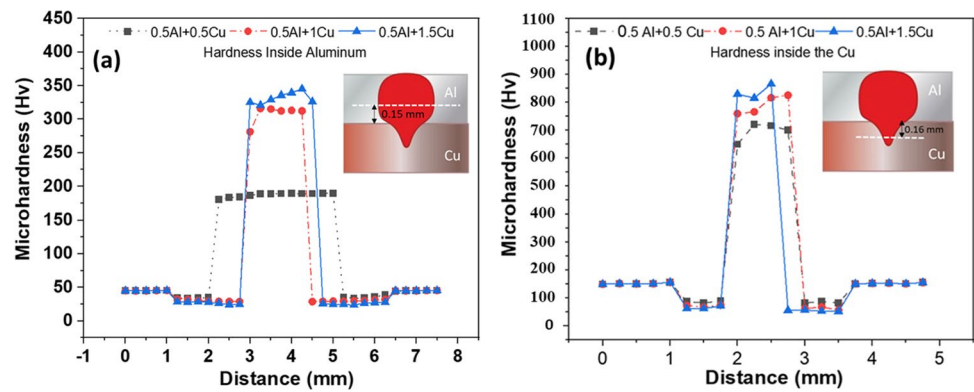
the hardness values were close to 320 Hv. But HAZ softening over a small width could be clearly observed for all three cases. The recrystallized grain structures and HAGB formation inside the weld, which can also be seen in the EBSD results, increased the hardness values to a greater extent. In the case of the bottom sheet where the Al penetrates inside the Cu, the increase in the hardness values was tremendously high. When welding a 1.5-mm bottom Cu sheet, the hardness value exceeded 800 Hv, which is the highest among the three cases. The lowest hardness value was obtained when welding a 0.5-mm thick bottom Cu sheet, which was almost 700 Hv. Welding a 1-mm thick bottom Cu sheet resulted in a hardness value of over 750 Hv. The accumulation of HAGB inside the Al penetrating Cu region, due to the formation of hard IMC phases, resulted in this tremendous increase in hardness values.

4 Conclusions

Successful joining between aluminum 1060 and pure copper could be achieved by laser welding. As the bottom Cu sheet thickness increased, the required volume energy input range for successful joining could be increased. This phenomenon further facilitated the joining of thicker bottom sheet plates with higher energy input, achieving high strength and improved electrical conductivity. The joining for all three cases was achieved by the diffusion of the Cu atoms inside the Al as the melted Al entered inside the bottom Cu plate during welding. Some of the key concluding points are summarized as follows:

- In the given range of volume energy input of 1.81–2.54, 2.18–3.18, and 5.73–7.64 KJ/mm^3, acceptable welding could be observed for bottom Cu sheet thickness of 0.5, 1, and 1.5 mm, respectively.
- Below the 1.81 KJ/mm^3 of volume energy input, only the formation of the weld bead took place on the aluminum plates, whereas no joining could be observed as the weld bead did not touch the copper surface. Any energy input

above 7.64 KJ/mm^3 generated significant observable macroscopic weld defects.

- Increasing 100% bottom Cu sheet thickness, the lowest amount of required volume energy increased to 20.44%, whereas the highest limit for the required volume energy increased by 25.19%.
- Increasing 200% bottom Cu sheet thickness by the lowest amount of required volume energy increased to 216.57%, whereas the highest limit of the required volume energy increased to 200.78%.
- The minimum depth of penetration of 0.18 mm was obtained in case of welding of 0.5-mm bottom Cu sheet, whereas for 1.5 mm, it was 0.65 mm, and for 1-mm thick bottom Cu sheet, it was 0.42 mm.
- The weld bead width gradually decreased as the bottom Cu sheet thickness increased. Hence, minimum weld bead width of 1.14 mm was seen for 1.5-mm bottom Cu sheet, whereas 1.27 mm of weld bead was formed for 0.5-mm bottom Cu sheet. Furthermore, in case of 1-mm bottom Cu sheet thickness, it is 1.19 mm.
- Inside the aluminum part, the highest possible hardness values of 350 Hv were observed for 1.5-mm bottom Cu sheet for 1-mm thick bottom Cu sheet; it mainly varied between 325 and 330 Hv. In the case of the 0.5-mm thick bottom Cu sheet, minimum hardness values of 200 Hv were obtained.
- Higher energy input facilitated a higher amount of Cu diffusion and mixing, forming copper-rich IMCs and enhancing the mechanical strength of the weld for bottom Cu sheet thickness of 1 and 1.5 mm.
- The highest breaking load of 373.59 N was observed for welding the bottom Cu sheet of a thickness of 1.5 mm, whereas the least breaking load of 244.02 was obtained for the 0.5-mm thick bottom sheet.
- In the case of the bottom sheet where the Al penetrates inside the Cu, the increase in the hardness values was tremendously high. When welding a 1.5-mm bottom Cu sheet, the hardness value exceeded 800 Hv, which is the highest among the three cases. The lowest hardness value was obtained when welding a 0.5-mm thick bottom Cu

sheet, which was almost 700 Hv. Welding a 1-mm thick bottom Cu sheet resulted in a hardness value of over 750 Hv

- The GBCD maps as obtained in the EBSD results clearly depict the formation of higher amount of HAGB for 1- and 1.5-mm thickness of bottom sheet Cu specially in those areas where the the presence of Cu is maximum.
- The EBSD, SEM, and EDS analyses pointed out the formation of IMC inside the weld by exhibiting Cu diffusion inside the weld and forming a fine-grained structure containing clusters of HAGB.

Declarations

References

1. Han J, Li S, Gao X, Huang Z, Wang T, Huang Q (2023) Effect of annealing process on interface microstructure and mechanical property of the Cu/Al corrugated clad sheet. J Mater Res Technol 23:284–299

2. Zhu Z, Shi R, Klarner AD, Luo AA, Chen Y (2020) Predicting and controlling interfacial microstructure of magnesium/aluminum bimetallic structures for improved interfacial bonding. J Magnes Alloy 8(3):578–586

3. Watanabe T, Takayama H, Yanagisawa A (2006) Joining of aluminum alloy to steel by friction stir welding. J Mater Process Technol 178(1-3):342–349

4. Chen S, Huang J, Xia J, Zhang H, Zhao X (2013) Microstructural characteristics of a stainless steel/copper dissimilar joint made by laser welding. Metall Mater Trans A 44(8):3690–3696

5. Zhao H, Debroy T (2001) Weld metal composition change during conduction mode laser welding of aluminum alloy 5182. Metall Mater Trans B 32:163–172

6. Shin WS, Cho DW, Jung D, Kang H, Kim JO, Kim YJ, Park C (2021) Investigation on laser welding of Al ribbon to Cu sheet: weldability, microstructure, and mechanical and electrical properties. Metals 11(5):831

7. Kaspar J, Zimmermann M, Ostwaldt A, Goebel G, Standfuß J, Brenner B (2014) Challenges in joining aluminium with copper for applications in electro mobility. MSF 783:1747–1752. https://doi.org/10.4028/www.scientific.net/msf.783-786.1747

8. Otten C, Reisgen UA, Schmachtenberg M (2016) Electron beam welding of aluminum to copper: mechanical properties and their relation to microstructure. Weld World 60:21–31

9. Yang J, Cao B (2015) Investigation of resistance heat assisted ultrasonic welding of 6061 aluminum alloys to pure copper. Mater Des 74:19–24

10. Wells P, Nieuwenhuis PA, Nash H, Frater LB. Lowering the bar: options for the automotive industry to achieve 80g/km CO2 by 2020 in Europe.

11. Achtnicht M, Von Graevenitz K, Koesler S, Löschel A, Schoeman B, Tovar Reaños MA (2015) Including road transport in the EU-ETS: an alternative for the future? ZEW Gutachten/Forschungsberichte

12. Lee SS, Kim TH, Hu SJ, Cai WW, Abell JA (2010) Joining technologies for automotive lithium-ion battery manufacturing: a review. Int Manuf Sci Eng Confer 49460:541–549

13. Shannon G, Chen H. Laser welding of aluminum and copper for battery welding applications using a 500W single mode fiber laser. In International Congress on Applications of Lasers & Electro-Optics 2009 2009, 1, pp. 1015-1020). Laser Institute of America.

14. de Leon M, Shin HS (2022) Review of the advancements in aluminum and copper ultrasonic welding in electric vehicles and superconductor applications. J Mater Process Technol 23:117691

15. Guo H, Hu J, Tsai HL (2009) Formation of weld crater in GMAW of aluminum alloys. Int J Heat Mass Transf 52(23-24):5533–5546

16. Cheng Z, Huang J, Ye Z, Chen Y, Yang J, Chen S (2019) Microstructures and mechanical properties of copper-stainless steel butt-welded joints by MIG-TIG double-sided arc welding. J Mater Process Technol 265:87–98

17. Ma T, Den Ouden G (1999) Softening behavior of Al–Zn–Mg alloys due to welding. Mater Sci Eng A 266(1-2):198–204

18. Hao X, Dong H, Yu F, Li P, Yang Z (2021) Arc welding of titanium alloy to stainless steel with Cu foil as interlayer and Ni-based alloy as filler metal. J Mater Res Technol 13:48–60

19. Liu F, Ren D, Liu L (2013) Effect of Al foils interlayer on microstructures and mechanical properties of Mg–Al butt joints welded by gas tungsten arc welding filling with Zn filler metal. Materials & Design 46:419–425

20. Cai ZP, Ai BQ, Cao R, Lin Q, Chen JH (2016) Microstructure and properties of aluminum AA6061-T6 to copper (Cu)-T2 joints by cold metal transfer joining technology. J Mater Res 31(18):2876–2887

21. Fan D, Yang N, Huang J, Yu X (2021) Plasma arc welding-brazing of aluminum to copper with SiO2 nanoparticles strengthening. J Manuf Proc 69:253–260

22. Feng J, Liu Y, Sun Q, Liu J, Wu L (2015) Microstructures and properties of aluminum–copper lap-welded joints by cold metal transfer technology. Adv Eng Mater 17(10):1480–1485

23. Genevois C, Girard M, Huneau B, Sauvage X, Racineux G (2011) Interfacial reaction during friction stir welding of Al and Cu. Metall Mater Trans A 42:2290–2295

24. Sahin M (2010) Joining of aluminium and copper materials with friction welding. Int J Adv Manuf Technol 49:527–534

25. Eslami P, Taheri AK (2011) An investigation on diffusion bonding of aluminum to copper using equal channel angular extrusion process. Mater Lett 65(12):1862–1864

26. Toroghinejad MR, Jamaati R, Dutkiewicz J, Szpunar JA (2013) Investigation of nanostructured aluminum/copper composite produced by accumulative roll bonding and folding process. Mater Des 51:274–279

27. Akca E, Gürsel A (2016) Solid state welding and application in aeronautical industry. Period Eng Nat Sci 4(1)

28. Mir FA, Khan NZ, Siddiquee AN, Parvez S (2022) Friction based solid state welding–a review. Mater Today: Proc 62:55–62

29. Kohn G, Greenberg Y, Makover I, Munitz A (2002) Laser-assisted friction stir welding. Weld J 81(2):46–48

30. Campanelli SL, Casalino G, Casavola C, Moramarco V (2013) Analysis and comparison of friction stir welding and laser assisted friction stir welding of aluminum alloy. Materials 6(12):5923–5941

31. Sun Z, Ion JC (1995) Laser welding of dissimilar metal combinations. J Mater Sci 30:4205–4214

32. Olabi AG, Alsinani FO, Alabdulkarim AA, Ruggiero A, Tricarico L, Benyounis KY (2013) Optimizing the CO2 laser welding process for dissimilar materials. Opt Lasers Eng 51(7):832–839

33. Ai Y, Shao X, Jiang P, Li P, Liu Y, Liu W (2016) Welded joints integrity analysis and optimization for fiber laser welding of dissimilar materials. Opt Lasers Eng 86:62–74

34. Attar MA, Ghoreishi M, Beiranvand ZM (2020) Prediction of weld geometry, temperature contour and strain distribution in disk laser welding of dissimilar joining between copper & 304 stainless steel. Optik 219:165288

35. Gedicke J, Mehlmann B, Olowinsky A, Gillner A (2010) Laser beam welding of electrical interconnections for lithium-ion batteries. In: International Congress on Applications of Lasers & Electro-Optics, vol 2010. Laser Institute of America, pp 844–849

36. Dimatteo V, Ascari A, Fortunato A (2019) Continuous laser welding with spatial beam oscillation of dissimilar thin sheet materials (Al-Cu and Cu-Al): Process optimization and characterization. J Manuf Process 44:158–165

37. Mathivanan K, Plapper P (2019) Laser welding of dissimilar copper and aluminum sheets by shaping the laser pulses. Procedia Manuf 36:154–162

38. Lerra F, Ascari A, Fortunato A (2019) The influence of laser pulse shape and separation distance on dissimilar welding of Al and Cu films. J Manuf Process 45:331–339

39. Berhe MG, Oh HG, Park SK, Lee D (2022) Laser cutting of silicon anode for lithium-ion batteries. J Mater Res Technol 16:322–334

40. Chatterjee S, Trinh LN, Lee D (2022) Mechanical and microstructural investigation of dissimilar joints of Al-Cu and Cu-Al metals using nanosecond laser. J Mech Sci Technol 36(8):4205–4211

41. Jarwitz M, Fetzer F, Weber R, Graf T (2018) Weld seam geometry and electrical resistance of laser-welded, aluminum-copper dissimilar joints produced with spatial beam oscillation. Metals 8(7):510

42. Lin R, Wang HP, Lu F, Solomon J, Carlson BE (2017) Numerical study of keyhole dynamics and keyhole-induced porosity formation in remote laser welding of Al alloys. Int J Heat Mass Transf 108:244–256

43. Huang L, Hua X, Wu D, Li F (2018) Numerical study of keyhole instability and porosity formation mechanism in laser welding of aluminum alloy and steel. J Mater Process Technol 252:421–431

44. Huang L, Hua X, Wu D, Ye Y (2019) Role of welding speed on keyhole-induced porosity formation based on experimental and numerical study in fiber laser welding of Al alloy. Int J AdvManuf Technol 103:913–925

45. Kutsuna M, Yan Q (1999) Study on porosity formation in laser welds of aluminium alloys (Report 2). Mechanism of porosity formation by hydrogen and magnetism. Weld Int 13(8):597–611

46. Tyagi T, Kumar S, Malik AK, Vashisth V (2022) A novel neuro-optimization technique for inventory models in manufacturing sectors. J Computational and Cognitive Engineering

47. Chen X, Shao X, Pan X, Luo G, Bi M, Jiang T, Wei K (2022) Feature extraction of partial discharge in low-temperature composite insulation based on VMD-MSE-IF. CAAI Trans Intell Technol 7(2):301–312

48. Gao X, Cao W, Yang Q, Wang H, Wang X, Jin G, Zhang J (2022) Parameter optimization of control system design for uncertain wireless power transfer systems using modified genetic algorithm. CAAI Trans Intell Technol 7(4):582–593

49. Aikhuele D (2023) Development of a statistical reliability-based model for the estimation and optimization of a spur gear system. J Comput Cogn Eng 2(2):168–174

50. Hust JG, Lankford AB. Thermal conductivity of aluminum, copper, iron, and tungsten for temperatures from 1 K to the melting point. National Bureau of Standards, Boulder, CO (USA). Chemical 1984.

51. Quintino L, Assuncao E (2013) Conduction laser welding. In: Handbook of laser welding technologies. Woodhead Publishing, pp 139–162

52. De A, DebRoy T (2005) Reliable calculations of heat and fluid flow during conduction mode laser welding through optimization of uncertain parameters. Weld J 84(7):101–112

53. Liu L, Wang H (2011) Microstructure and properties analysis of laser welding and laser weld bonding Mg to Al joints. Metall Mater Trans A 42:1044–1050

54. Fortunato A, Ascari A (2019) Laser welding of thin copper and aluminum sheets: feasibility and challenges in continuous-wave welding of dissimilar metals. Lasers Manuf Mater Process 6:136–157

55. Zhou L, Li GH, Zhang RX, Zhou WL, He WX, Huang YX, Song XG (2019) Microstructure evolution and mechanical properties of friction stir spot welded dissimilar aluminum-copper joint. J Alloys Compd 775:372–382

56. Schmalen P, Plapper P, Peral I, Titov I, Vallcorba O, Rius J (2018) Composition and phases in laser welded Al-Cu joints by synchrotron x-ray microdiffraction. Procedia CIRP 74:27–32

57. Chen CY, Chen HL, Hwang WS (2006) Influence of interfacial structure development on the fracture mechanism and bond strength of aluminum/copper bimetal plate. Mater Trans 47(4):1232–1239

58. Hou W, Shah LH, Huang G, Shen Y, Gerlich A (2020) The role of tool offset on the microstructure and mechanical properties of Al/Cu friction stir welded joints. J Alloys Compd 825:154045

59. Jiang HG, Dai JY, Tong HY, Ding BZ, Song QH, Hu ZQ (1993) Interfacial reactions on annealing Cu/Al multilayer thin films. J Appl Phys 74(10):6165–6169

60. Lee WB, Bang KS, Jung SB (2005) Effects of intermetallic compound on the electrical and mechanical properties of friction welded Cu/Al bimetallic joints during annealing. J Alloys Compd 390(1-2):212–219

61. Dehghan-Manshadi A, Hodgson PD (2008) Dependency of recrystallization mechanism to the initial grain size. Metall Mater Trans A 39:2830–2840